

Magnetic Actuation System Dataset Generation and Characterization

Gediyon Moges Girma

Supervisors: Dr. Eric Diller, Daniel Sieben, Erik Fredin

August 2024

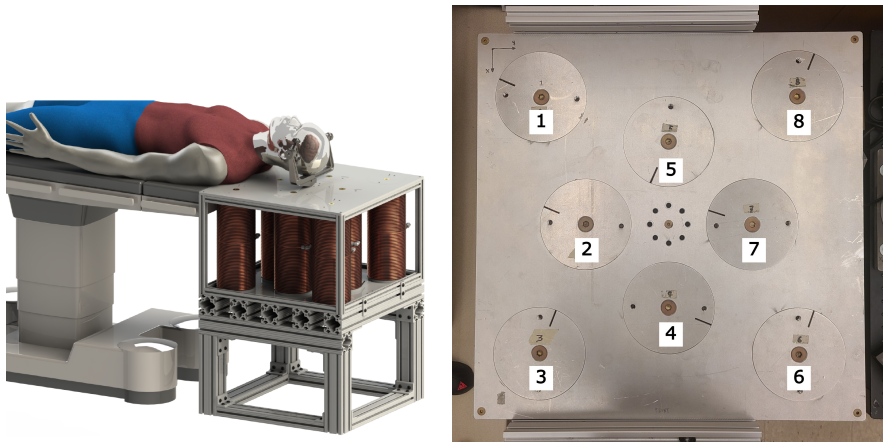
1 Introduction

The Micro-robotics lab at the University of Toronto has developed an 8-coil magnetic actuation system designed for use with magnetic medical instruments. The system generates a magnetic field to control surgical tools while serving as an operating table. Currently, the magnetic field generated by the system has only been calibrated for a small workspace around the center of the table.

In practice, surgical tools are required to operate across the entire 3D workspace above the operating table. To ensure effective operation in this space, the magnetic field generated by the system needs to be well-understood and controlled in all areas, not just at the center. This requires quantifying the magnetic field through measurement over the entire workspace of the coil table. The collected data will then be used to refine the existing model and develop an improved one using machine learning techniques for better control. This project focuses on measuring the 3D magnetic field generated by the coil system to achieve these goals.

2 Magnetic Actuation System

The magnetic actuation system has been developed for minimally invasive neurosurgery [1]. It maximizes the workspace accessibility without hindering neurosurgeons' ability to intervene at any stage of the operation. It also generates a strong enough magnetic field to effectively actuate the surgical tools. The actuation system consists of 8 coils that can produce a magnetic field up to 38mT in the x and y direction and 47mT in the vertical direction at the center of the table 12cm from the surface. A rendering of the actuation system is shown in Figure 1a.



(a) Magnetic actuation system rendering [1] (b) Top surface of the actuation system with coil labels

Figure 1: The magnetic actuation system

The top flat surface of the system measures $610mm \times 610mm$, with the electromagnetic coils placed below. Figure 1b shows the top surface of the actuation system with labels for each electromagnetic coil. As shown in the figure, a coil is placed at each corner of the table and the rest are clustered around the center. The coils are arranged symmetrically with respect to the vertical planes $x = 0$, $y = 0$ as well as the diagonal planes $x = y$ and $x = -y$.

Each coil contains of a cast iron core inside measuring 90mm in diameter and 360mm in length (aspect ratio of 8) wrapped by ten layers of 12 gauge ($3.31mm^2$) wire each of which is roughly around 163 turns (1630 turns per coil). A current density of $6A/mm^2$ is found to be feasible for power input which indicates a current input range of $\pm 20A$. The coil's electrical resistance produces significant heat, so the system is cooled using water from a nearby tap. To monitor the core temperature and prevent overheating, each coil is equipped with a thermocouple sensor placed in between the coil wires the core.

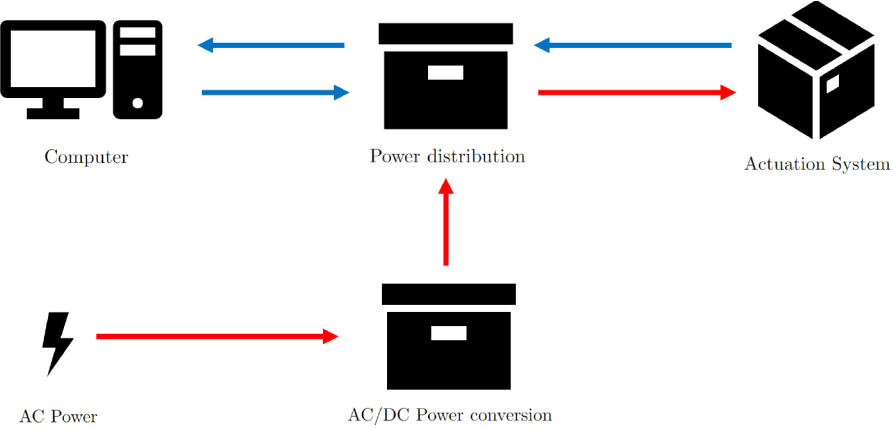


Figure 2: Magnetic actuation system layout, Signal lines are indicated in blue and power lines are indicated in red

2.1 System Design Description

As illustrated in Figure 2, the system layout consists of four separate units: a computer, power distribution unit, AC/DC converter, and the coil system. The AC/DC converter converts the AC power from the grid to a DC power and supplies it to the power distribution unit. The power distribution unit contains 8 AB50A100 servo drivers that receive a command signal voltage from the computer, map it to a DC current and supply it to the electromagnetic coils in the actuation system. In return, the actuation system sends temperature readings back which is passed on to the computer along with the feedback signal for the supplied current.

2.2 The Dipole Model

The magnetic moment of a permanent magnet can be described in terms of its residual magnetism \mathbf{B}_r and its volume V as follows:

$$m = \frac{1}{\mu_0} B_r V \quad (1)$$

The magnetic field generated at distance r with magnetic moment can be approximated by the dipole model in equation 2.

$$B_{dip}(r) = \frac{\mu_0}{4\pi \|r\|^3} [3(m \cdot \hat{r})\hat{r} - m] \quad (2)$$

For electromagnets, the magnetic field generated depends on the current supply and for any point p , it is described by Biot-Savart law [2]. As can be seen in equation 3, it is computationally intensive to solve. However, it can be observed that the magnetic field produced is linearly dependent on the applied current for this theoretical case where the effect of the core material is being neglected.

$$B(p) = \frac{\mu_0}{4\pi} \int_C \frac{Id\mathbf{I} \times \mathbf{r}}{\|r\|^3} \quad (3)$$

where, $\mathbf{r} = \mathbf{p} - \mathbf{L}$ is the relative position vector from the current element $d\mathbf{L}$ to the point of interest \mathbf{p} .

As long as the core material is soft and does not reach its magnetic saturation point, it should respond linearly to input current but when tested the cast iron cores were exhibiting non-linearity above $3.5A/mm^2$ current density [11A][1]. Nonetheless, a linear assumption was taken for both magnetic field strength and magnetic field gradient in order to calculate torque and force on a magnetic surgical tool respectively (refer [1] for detailed formulation).

3 Previous System Calibration

Schonewille [1] has done a single point calibration at the origin point using a Gauss probe on a 3D axis gantry. The magnetic field gradient was measured by moving the gantry 1.86mm in the three principal axis and taking another measurement to numerically calculate the gradient. The magnetic field vs current plot produced for each coil shows that there is no magnetic hysteresis but linearity falls off above a certain limit. The results for the magnetic field gradient were also clearly shown to be noisy and non-linear yet all results was approximated to be linear. This assumption allows us to calculate the needed current supply for the required magnetic field by taking the inverse of linear coefficient matrix, $\mathcal{U}(p)^{-1}$, of equation 4 [1].

$$\begin{bmatrix} B(p) \\ G(p) \end{bmatrix} = \begin{bmatrix} \mathcal{B}(p) \\ \mathcal{G}(p) \end{bmatrix} I = \mathcal{U}(p)I \quad (4)$$

Where, $B(p)$ and $G(p)$ predicted magnetic field and gradient respectively, $\mathcal{B}(p)$ and $\mathcal{G}(p)$ is linear coefficients obtained from calibration, I is applied current.

Although a model was synthesized from the preliminary calibration data for the origin point, re-calibration of the actuation system for the entire 3D space above the table is found to be necessary. In the following section of the report, the objective of the this project, the approach and result of this project are outlined.

4 Objectives

The main objectives of this project are to

1. Generate a 3D magnetic field measurement dataset for a given current input suitable for training a machine learning model.
2. Determine the bias of the dipole model for the 3D space around the system.

4.1 Specific Objectives

The specific objectives of this project include:

1. Planning and setting up an experiment to measure the magnetic field generated by the coil actuation system using Franka Emika robot arm for precise spatial control of the magnetic flux sensors. The planning of the experimental system includes:
 - Identification of sources of measurement uncertainty
 - Explore ways to enhance the quality of the data by minimizing measurement uncertainty.
2. Investigation of the electrodynamic interaction between multiple coils of the magnetic actuation system.

5 Approach

To measure the field across the entire workspace, a method for moving the sensors in a consistent and repeatable manner is necessary. In this project, a Franka Emika robot arm is used to repeatedly move the sensors over the 3D workspace above the actuation system. The magnetic field measurement will be conducted for differred current supply to fully characterize the system.

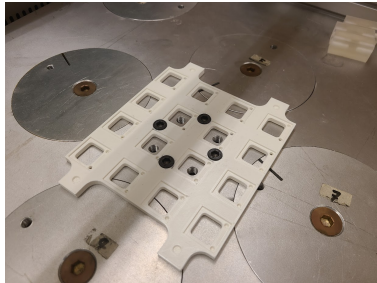
The other important consideration is the type of magnetometer used to measure the fields generated. MLX90393 IMU magnetometers are the primary sensors and Model 460 Gauss is used to verify the measurement. Sensor specification for both sensors are given the Appendix. For the sake of time efficiency, the magnetic field will be measured at 16 positions simultaneously with an array of magnetic flux sensors.

5.1 Sensor Array

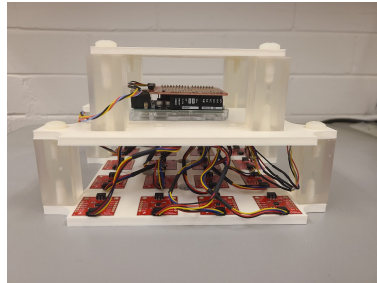
A sensor array designed by a previous summer student [3] was modified to a more sturdier structure and precise arrangement of individual sensors. The new design, as can be seen in Figure 3, has three layers separated by four corner pillars. All layers are 3D printed using Ultimaker 3D printer while the pillars are reused from the previous design which were 3D printed using Form-labs form3 3D printer.

The bottom layer, shown in Figure 3a, has cutouts for each magnetometer sensors to precisely orient, align, and arrange them in a 4×4 manner. In addition, it also has a cut out to position the sensor array to our reference position (new origin point) by snapping-on to four anchor points. The anchor points are bolt heads that protrude out of the top surface of the actuation system and they set the horizontal plane position and orientation of the sensor array while the actuation system's top surface set the vertical position and orientation.

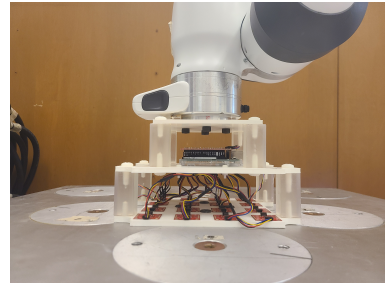
The mid-layer holds the Arduino Uno microcontroller and accessory break-out boards for the sensors. And the top layer has attachment holes that securely attaches the sensor array to the Franka-Emika robot arm. Figure 3b and 3c shows the sensor array from different angles with and without the robot arm attached respectively.



(a) Bottom layer of the sensor array structure at reference position.



(b) Side view of the sensor array structure



(c) Sensor array attached to a robot arm at the reference position

Figure 3: The sensor array

The spatial resolution of our measurement is set by the sensor array that is 40mm interval in the three principal axis. The 3D space monitored was limited by the reach of our robot to be $420\text{mm} \times 420\text{mm} \times 280\text{mm}$ volume of space.

5.2 Measurement Uncertainty

The measurement uncertainty for this project can be classified into two. The first one is spatial uncertainty that is related to location of our sensor relative to the actuation table. The second one is the uncertainty related to the measurement accuracy of our sensors.

5.2.1 Spatial Uncertainty

The spatial uncertainty is mainly attributed to the robot arm's movement. Other source of uncertainties such as the print resolution of the Ultimaker 3D printer (± 6.9 microns) and caliper measurements done (± 20 microns) is very small by comparison thus can be neglected. The robot arm's pose repeatability is ± 0.1 mm [4]. Although very small, that is the biggest source of spatial uncertainty on our measurement.

5.2.2 Magnetic Field Measurement Uncertainty

The MLX90393 sensor is highly sensitive to change in magnetic field down to $3.22\mu\text{T}/\text{LSB}$ on the horizontal axis and $5.672\mu\text{T}/\text{LSB}$ on the vertical axis. That is a very fine resolution, more sensitive than the Model 460 Gaussmeter, with plenty of range for our application. The sensors accuracy (conformance to the true value) has been verified with the model 460 Gauss-meter before data collection started and shown in Figure 4 and 5.

The verification was conducted for three runs (tests) by generating a single axis dominated field for each runs. Fields in the z, x and y axis is used for test 1,2 and 3 respectively. The plots show that the error in the z-axis is lower than in the x-axis which is lower than the y-axis fields. The maximum percent error is about 7% for test 3 and just below 5% for test 1. The absolute error is given in Figure 5 and it shows the maximum error to be about 0.8mT for test 3 while it is only about 0.4mT for test 1. The sensor verification results indicate higher than expected difference between our sensor array (MLX90393 sensors) and Gauss-meter measurements but it is moderately acceptable for our case.

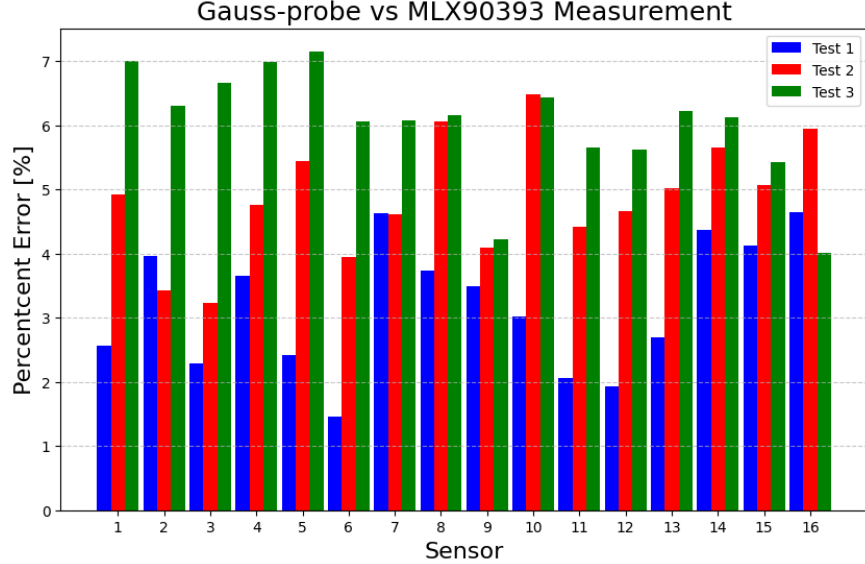


Figure 4: Percentage error of MLX90393 relative to Gauss-probe measurement

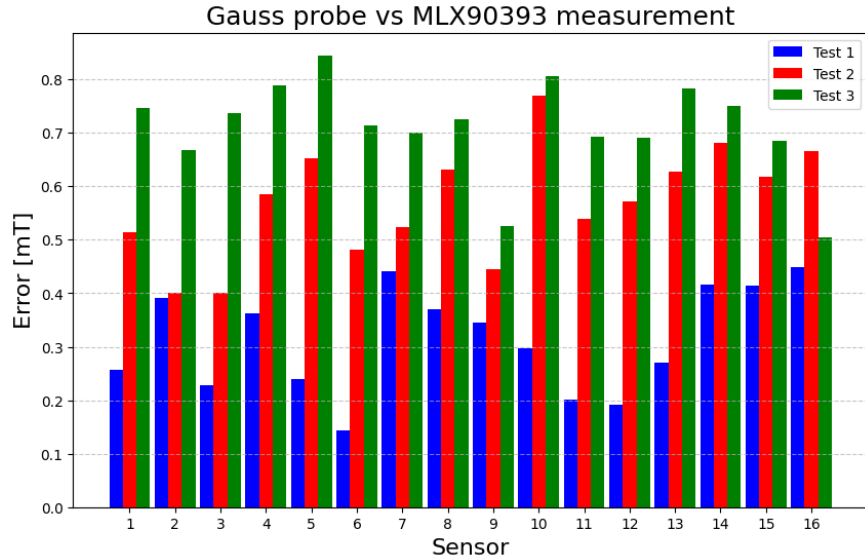


Figure 5: Measurement difference in mT of MLX90393 relative to Gauss-probe measurement

5.3 Coil Temperature

As current flows through the coil, the core material heats up and thus affects the magnetic field generated by the coil system. The current cooling method is not designed to keep the core temperature at a constant temperature during operation. This will lead to temperature fluctuation over time. Given the supply current stays the same, the core temperature will eventually stabilize at a certain equilibrium temperature. Ideally, measurements should be taken after the temperature has stabilized. But the time it takes for stabilization limits its practicality.

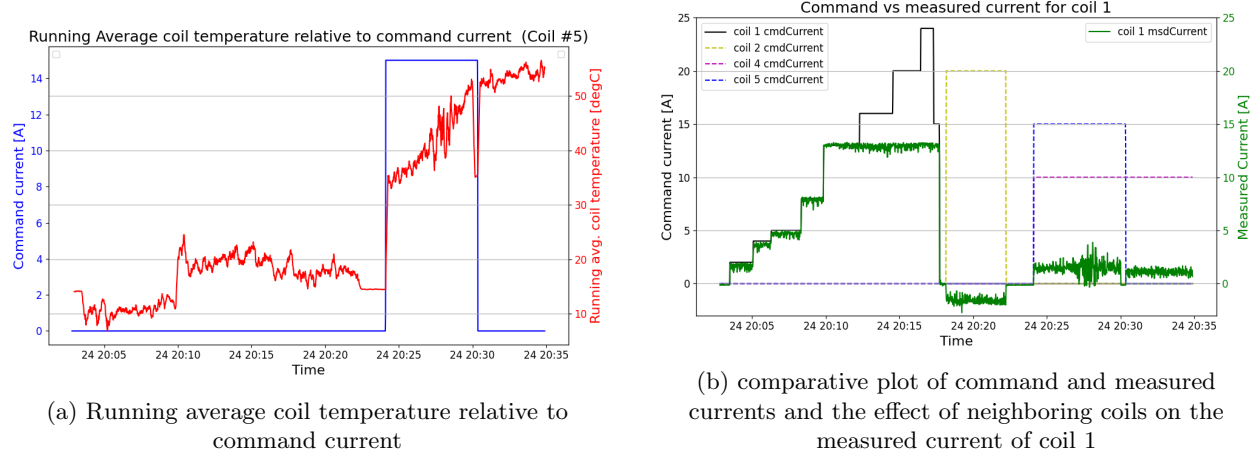


Figure 6: Preliminary data plots

Figure 6a illustrates the 10-second running average of coil temperature (in red) and command current (in blue) plotted against time. The running average temperature is represented on the left vertical axis, while the command current is plotted on the right vertical axis. The plot reveals a notable spike in temperature immediately upon the application of current. Subsequently, the temperature rises steadily until the current is removed, at which point a sudden flicker is observed. This flicker is followed by a noticeable sign of temperature reversal, indicating cooling of the core material.

The thermal probe, positioned between the core and the winding (the heat source) [1], measures the temperature of the winding coils or the outer surface of the core. This placement explains the abrupt temperature spikes observed with the application or removal of current. The core material requires some time to reach thermal equilibrium and waiting for it to reach that equilibrium after every current setting is unpractical for our measurements. The temperature rise after the initial spike is approximately 15 °C over roughly 10 minutes and this temperature rise will slow down as time goes on. This rise can be assumed to not significantly alter the core material properties to affect the generated magnetic field for our use case.

5.4 Linearity of magnetization

The actuation system has a current input limit of $\pm 24\text{A}$. From previous calibration of the system by A. Schonewille [1], the magnetic field generated is linear in $\pm 15\text{A}$ input range. Linearity implies the generated magnetic field is linearly correlated with the input current.

Our current supply however is limited to only $\pm 13\text{A}$ regardless of the command current amount specified outside of that range. Figure 18b shows the command current versus the measured current for a sample coil, coil #1. As shown in the plot, the measured current precisely tracks the command current up to 13A, and it will stay at 13A for all command currents above 13A. This ensures that our system is only operating in the linear range of magnetization.

Command currents for nearby coils are also plotted to show how the other coil's magnetization affects the measured current of coil #1. After coil #1's command current is set to zero, when coil #2 is magnetized, as shown by its command current, the measured current of coil #1 shifts from 0A to around -2A. The same behaviour can be observed when coil #4 and #5 is simultaneously magnetized. This indicates that the magnetization of a coil creates current flow in the neighbouring coils.

5.5 Measuring Sweeps

The continuous current input space in the linear range needs to be discretized to take measurements at discrete input values. Because the linear magnetization can be simply described by a linear formulation or represented by a straight line, coarse sampling is sufficient to represent the relationship. As a result a sampling interval of 2A is chosen for our measurement.

Considering every permutation of the input current for each coil in the linear range, over 2.5 billion sweeps of the 3D space is required. This amount of sweeps is too high to achieve with the time and resources available. According to Kummer et al. [5], a method of superposition can be adopted as long as the core of each electromagnet operate in its linear magnetization region. Superposition is a method of independently measuring the generated magnetic field for each coil and combine them by addition to get the combined effect. This will allow us to compute the full discrete input space data (over 2.5 billion sweeps worth) with just 120 sweeps. For verification, 3 sweeps with a random combination of current inputs have been measured and compared with the superimposed data.

5.6 Robot Control

When it is desired to move the robot tip (or end effector, EE) to a desired position P relative to the actuation table T, the robot controller expects a command position relative to the robot base O. The naming convention used in this project is shown in Figure 7. To convert the relative position from the actuation table frame to the robot base frame we need a transformation matrix T_{TO} and it can be calculated from intermediate transformation matrices as described in Equation 5.

When setting the initial reference position for the sensor array, we obtain the transformation matrix T_{OE} that transforms a position vector from the end effector frame to the robot base. T_{OE} can be represented by equation 6 where C_{OE} is the rotational component and r_o^{EO} is the translational component. By taking the inverse of T_{OE} we obtain T_{EO} as shown in Equation 7. Similarly, T_{TE} can be easily obtained by rotating the x and z axis by π and $\pi/4$ respectively, and moving the origin point 0.1064 m in the z-direction which is the distance from the actuation system surface to the robot arm tip (EE) at reference position (refer to Figure 3a).

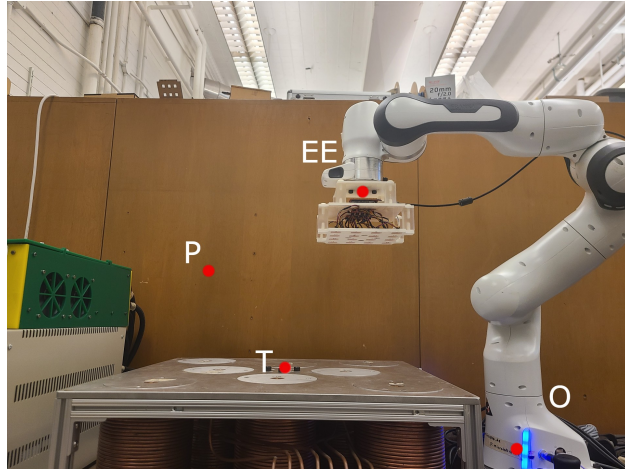


Figure 7: Naming convention for robot control

$$T_{TO} = T_{TE} T_{EO} \quad (5)$$

$$T_{OE} = \begin{bmatrix} C_{OE} & r_o^{EO} \\ 0^T & 1 \end{bmatrix} \quad (6)$$

$$T_{EO} = T_{OE}^{-1} \quad (7)$$

$$T_{TE} = \begin{bmatrix} I^{3 \times 3} \cdot C_x(\pi) \cdot C_z(\pi/4) & r_T^{ET} \\ 0^T & 1 \end{bmatrix} = \begin{bmatrix} \frac{\sqrt{2}}{2} & \frac{\sqrt{2}}{2} & 0 & 0 \\ -\frac{\sqrt{2}}{2} & \frac{\sqrt{2}}{2} & 0 & 0 \\ 0 & 0 & -1 & 0.1064 \\ 0 & 0 & 0 & 1 \end{bmatrix} \quad (8)$$

where, $r_T^{ET} = [0, 0, z_{ref}]^T = [0, 0, 0.1064]^T$

Once T_{TO} is calculated, we can convert the positional feedback signal from the robot to position vectors relative to the table reference frame ($r_T^{PT} = T_{TO} \cdot r_O^{PO}$) for data collection and vice versa to send a command to the robot ($r_O^{PO} = T_{TO}^{-1} \cdot r_T^{PT}$). Using the formulation above, the robot has been programmed to move to a 3D grid point positions with 160mm interval in the horizontal axis and 40mm in the vertical axis so that the sensor array can cover 440mm \times 400mm \times 280mm space.

5.7 Automation and data collection

Robot automation and data collection has been implemented on top of an in-house developed program. The program is written in C++ language in the Qt environment. For this project, a new calibration interface (GUI window) was added for ease of use. The Calibration window can be launched from the main window which is shown in red box in Figure 14 in the appendix. The main window interface was used to set command current values shown in Green box in Figure 14.

The code uses a multi-threading configuration for sending the robot command and data collection. The basic working principle is that a worker thread keeps the rhythm of data collection by sending a new position command to the main thread every 4 seconds. A function in the main thread performs the transformations and pass the command to the robot controller to have the movement completed in 2 seconds. After successfully reaching the destination data will be collected for the remaining 2 seconds before a new command is received to move to a new grid location.

The program ensures that every grid point is visited per sweep one after the other in the 3D grid of measuring space. The 3D sweep begins once the robot is positioned at the initial position. The robot moves to the initial position by clicking "Move robot to initial position" in Calibration Window then click "start 3D sweep" to start measurement (refer Figure 15). Other functionalities such as moving the robot tip relative to the current location; starting, stopping or pausing recording; setting reference position to calculate T_{TO} and moving the Gauss probe to the old "origin position" has been provided in the calibration window.

The data collected from the calibration window include each sensor's location relative to the table frame, command current, feedback current, coil temperature and homogeneous transformation matrix T_{OE} . Magnetic flux measurements were collected separately with a python script to be merged in post-processing based on the timestamp of the data.

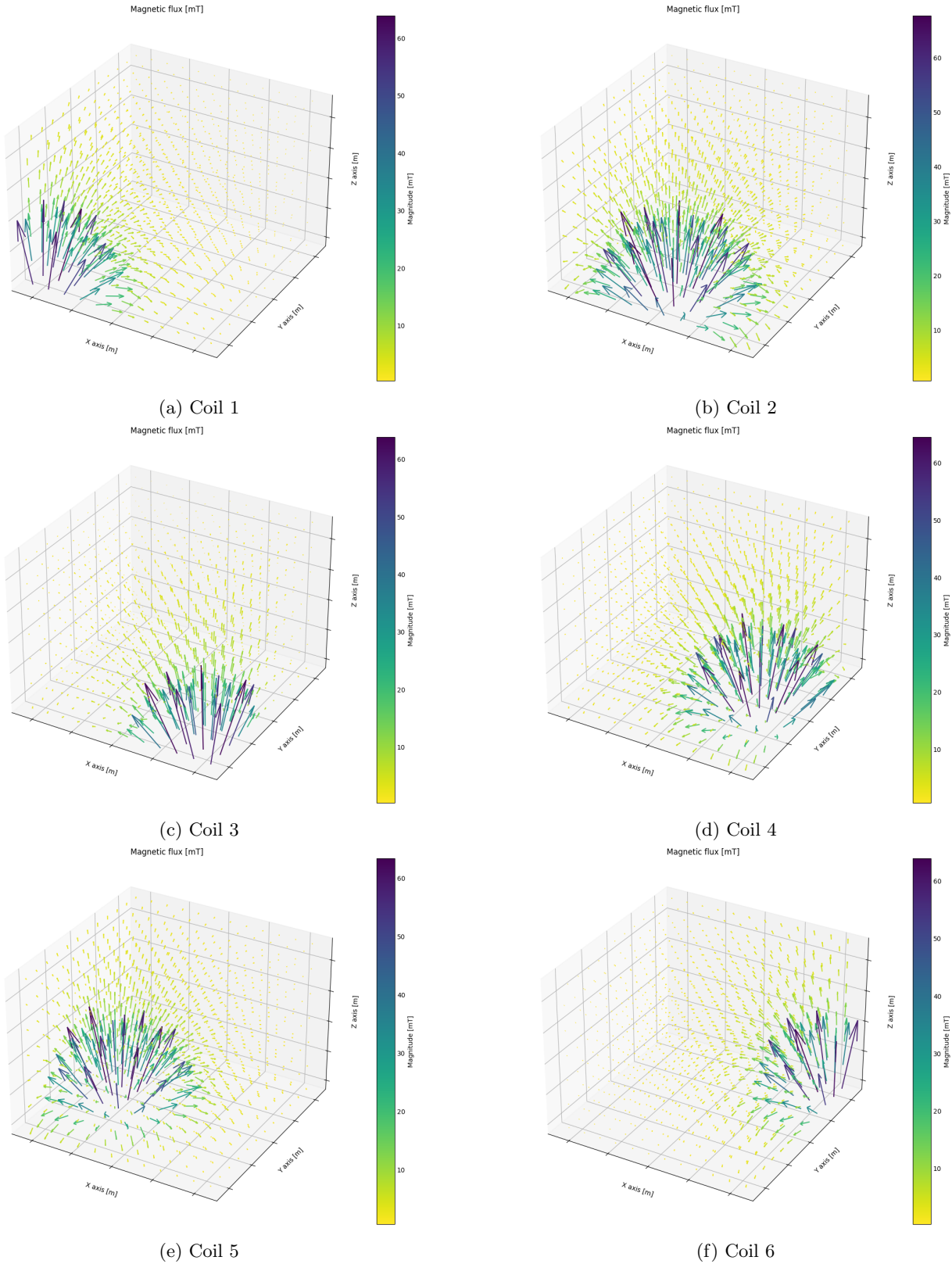
6 Result and Discussion

The data collected through our GUI interface and python script have been processed and stored ready to be used to train a machine learning model. The data processing includes merging the data, and calculating the mean for each grid point. The processed data for each coil is visualized in Figure 9 for an input current value of +13A. Although coil 6 was out of service during measurement, its data was generated by leveraging symmetry, specifically by reflecting coil 8's measurement across x-z plane. This has been shown in Figure 8f.

Figure 9 shows that intense magnetic field is generated by each coil that is a little bit over 60mT near it. The generated field exponentially decays away from the center of the coils. Another interesting fact to note is that the magnetic field is slightly more intense at the periphery than at the center which is shown more clearly in the sectional views presented in Figure 10.

6.1 Superpositioning

To assess how well super-positioning performs compared to direct measurement, we conducted three test measurements of complex magnetic fields generated by energizing multiple coils. The measured results are then compared them with the superimposed data from our dataset. The three test cases were as follows:



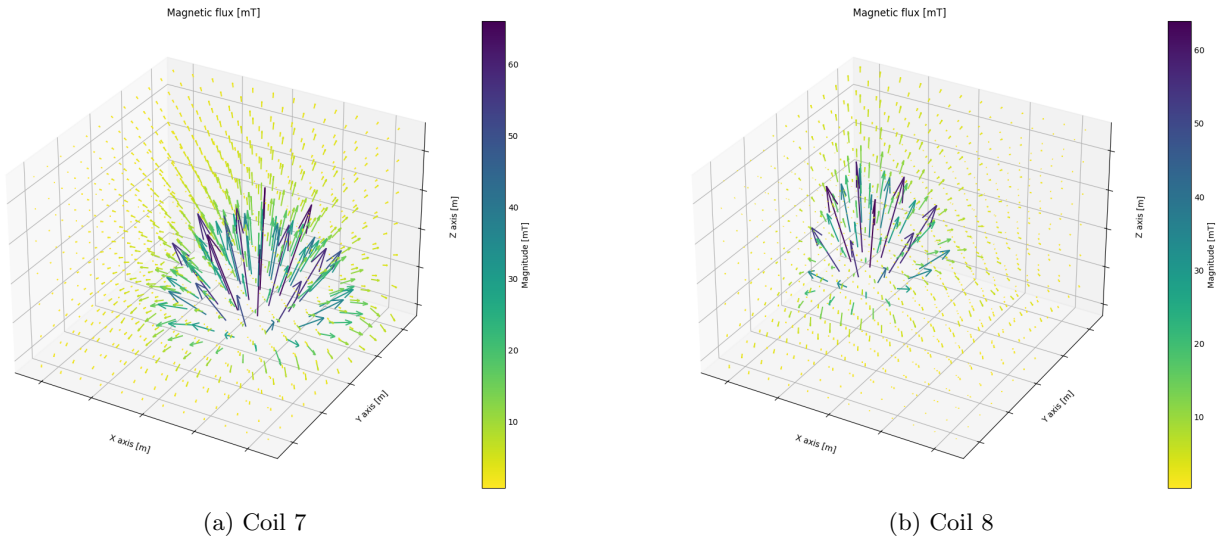


Figure 9: Measured magnetic field plot for command current of 13A

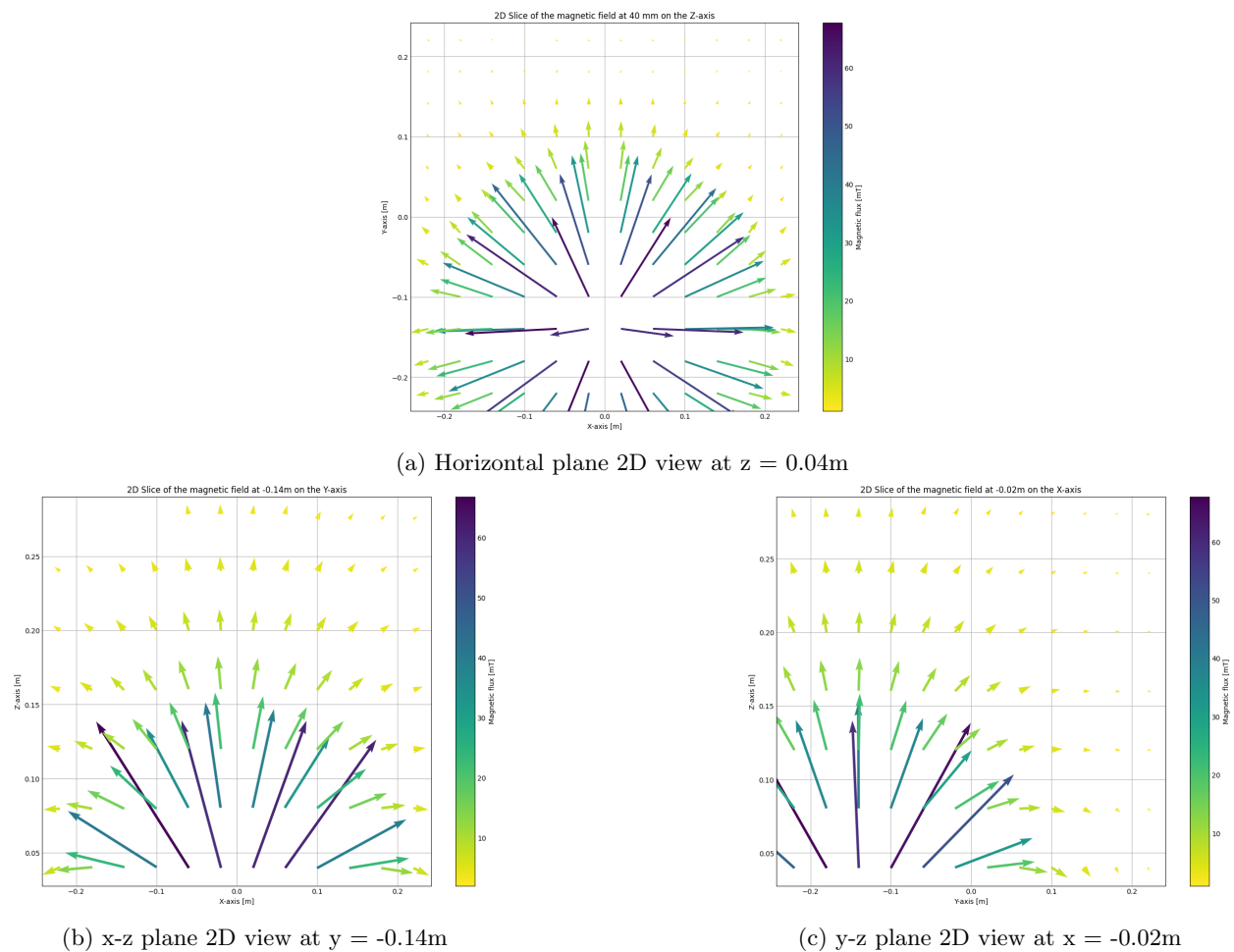


Figure 10: vertical and horizontal section views of magnetic field generated by coil 2 by command current of 13A

- Test 1 is a magnetic field mainly in the positive z direction with input current of 5A for all coils except coil 6.
- Test 2 is magnetic field mainly in the positive x direction with input command current of [10, 0, -10, -5, 5, 0, 0, 10] for coil 1 to 8 consecutively.
- Test 3 in the positive y-direction with input command current of [-10, -5, -10, 0, 0, 0, 5, 10] for coil 1 to 8 consecutively.

Figure 11 shows the comparison between the superimposed and measured data for Test 1, while comparison plots for Tests 2 and 3 are presented in Appendix C. Note that the superimposed data for test 2 and 3 is obtained by linear interpolation from the dataset. Different color schemes were used to distinguish between the measured and superimposed data. In all cases, the visual similarity between the two data sets demonstrates our superposition technique's validity.

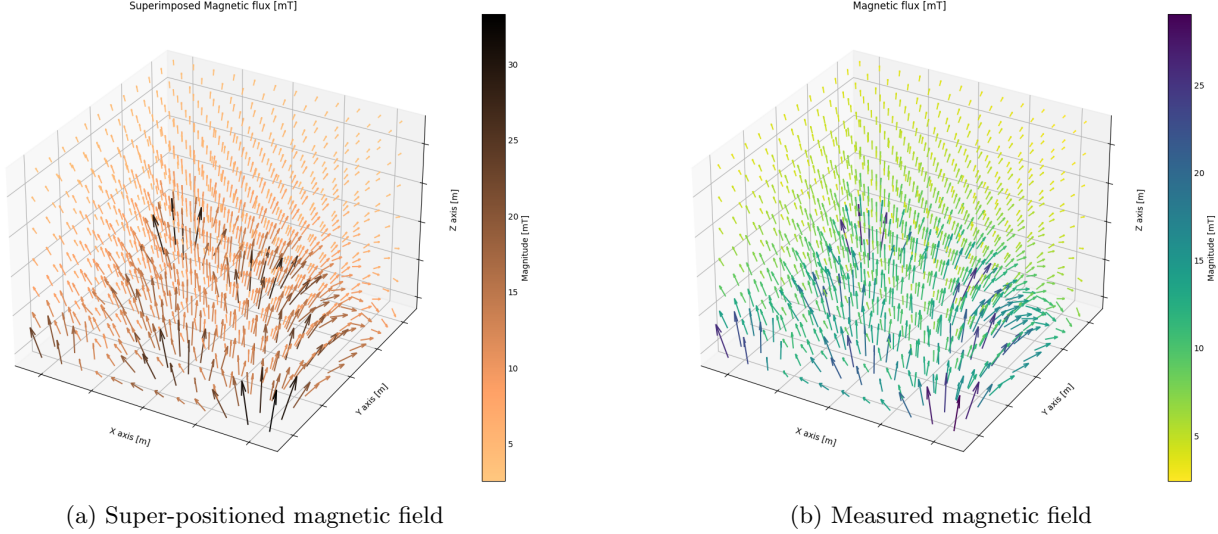


Figure 11: Super-positioned vs measured magnetic field test 1.
Input command current = [5, 5, 5, 5, 5, 5, 0, 5, 5] for coil 1 to 8 consecutively

To quantify the accuracy of the superimposed magnetic field, mean absolute error (MAE) and Mean absolute percent error (MAPE) is calculated and presented in Table ???. The mean absolute error indicates the difference between the two magnetic fields in absolute terms in mT while the percentage absolute error provides perspective into how big the difference is with respect to the measured value. The table also provides the error measure for orientation. The orientation of the magnetic field can be described by two angles which are pitch angle ϕ (the angle between the magnetic field and the horizontal plane) and yaw angle θ (the angle in the horizontal plane from the positive x-axis).

The MAE for the field as well as pitch angle is shown to be slightly higher for the interpolated data of test 2 and test 3 than the non interpolated data. The interpolated data was produced from the 12 field measurement for a single coil while the non interpolated data (test 1) used only 7. Due to the additional calculation step and amount of data, more errors are introduced into the super-positioned field.

For test 1, the MAPE of the resultant or magnitude of the magnetic field is 4.6% which is acceptable. However the error in the x and y orientation is substantial with the average percent error of 42.2% in the x-axis and 106.4% in the y-axis. (1.47°). Similarly, the MAPE in the x direction is found to be far less than the other dimension for test 2 which happen to have x-axis dominant magnetic field. The same characteristic can be seen for test 3 but in the y-axis. This indicates that the error is more pronounced in smaller field direction than the dominant field direction.

In all test cases, the vertical magnetic field is shown to be more error prone than the horizontal direction fields as shown in MAE calculations. And the error in the magnetic field orientation is seen to be higher for

the yaw angle (θ) than the pitch angle (ϕ) with the yaw angle error staying relatively constant for all test cases.

| Direction/ Orientation | Test 1 | | Test 2 | | Test 3 | |
|------------------------|----------|----------|----------|----------|----------|----------|
| | MAE [mT] | MAPE (%) | MAE [mT] | MAPE (%) | MAE [mT] | MAPE (%) |
| X | 0.27 | 42.2 | 0.52 | 25.1 | 0.51 | 125.7 |
| Y | 0.26 | 106.4 | 0.47 | 82.5 | 0.45 | 22.2 |
| Z | 0.42 | 6.1 | 0.92 | 61.3 | 0.96 | 118.8 |
| Field magnitude | 0.44 | 4.6 | 0.77 | 6.9 | 0.68 | 6.1 |
| $\phi(^{\circ})$ | 1.47 | | 3.92 | | 4.5 | |
| $\theta(^{\circ})$ | 5.06 | | 4.90 | | 5.0 | |

Table 1: Mean absolute and mean absolute percentage error between the superimposed and measured magnetic fields

6.2 Dipole model prediction vs measured dataset

Three dipole models were considered for predicting the actuation system's magnetic field. A model with two dipoles located at the centre of the top and bottom half of a coil was found to be more accurate in its prediction than a single dipole at the surface of the table or at the the coil's centeroid. Hence, the following discussion is about a model with two dipoles at -90mm and -270mm in the z direction for each coil. The cast iron relative magnetic permeability is estimated to get close result to the measured values.

The prediction error of the dipole model against the command current for a sample coil (coil 2) is shown in Figure 12 and plots for all other coils is given in Appendix D. Figure 12 shows that the model prediction error rises linearly with command current. The model is shown to be accurate with maximum error of around 0.7mT for $\pm 13A$ current input.

The orientation MAE for both pitch and yaw angle did not show any noticeable pattern with the input current values. The orientation error stayed relatively low for all input currents but a sudden spikes is noticed when the input current values are close to zero. The exact reason for the spike is not clear and further investigation is required.

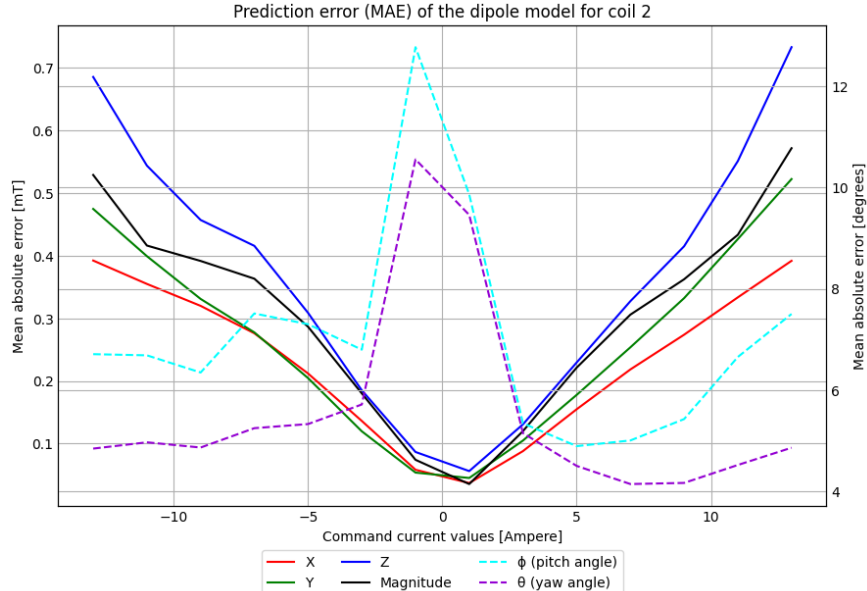


Figure 12: MAE of the dipole model predication for coil 2

For complex magnetic fields created by energizing multiple coils, the dipole model produces a similar field as compared with the measured data as shown in Figure 13 and in appendix C. However, when computing the MAE and MAPE values, as shown in Table 2, the results are more than expected. The mean absolute error ranges from 3mT to up to 10.42mT. The orientation is similarly off by at least 20° and up to 58° on average. This indicates that the dipole model needs further tweaking for better results and perhaps a better model should be considered, such as an ML model, that can accurately represent the generated magnetic field.

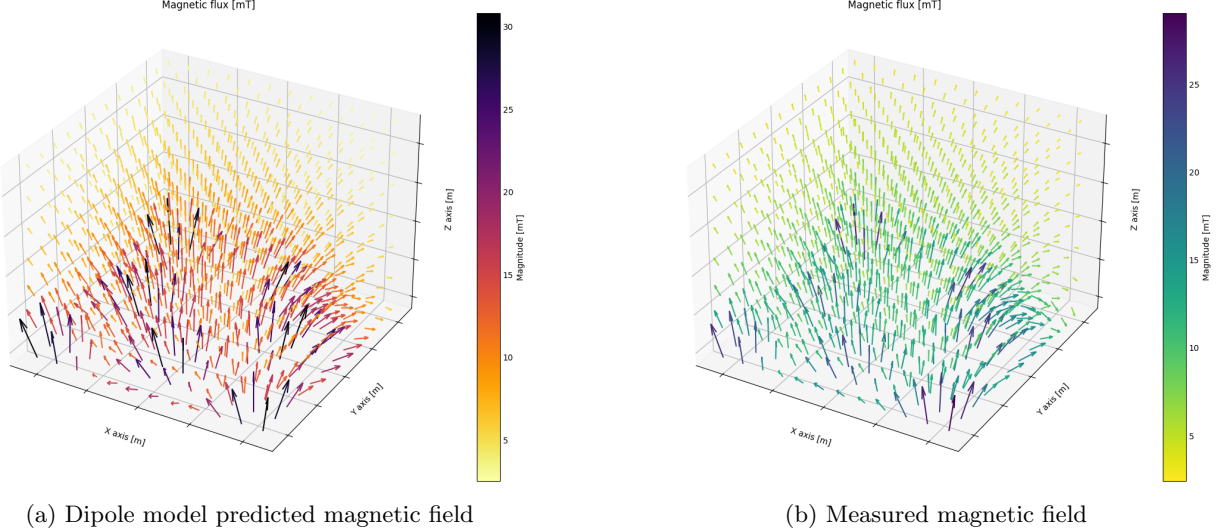


Figure 13: Simulated vs measured magnetic field test 1.
Input command current = [5, 5, 5, 5, 5, 0, 5, 5] for coil 1 to 8 consecutively

| | Test 1 | | Test 2 | | Test 3 | |
|--------------------|----------|----------|----------|----------|----------|----------|
| | MAE [mT] | MAPE (%) | MAE [mT] | MAPE (%) | MAE [mT] | MAPE (%) |
| X | 4.04 | 758 | 6.40 | 346 | 2.93 | 597 |
| Y | 3.97 | 1400 | 3.07 | 680 | 6.55 | 405 |
| Z | 4.76 | 138 | 10.42 | 549 | 10.32 | 689 |
| Field magnitude | 5.09 | 73 | 8.61 | 103 | 8.7 | 107 |
| $\phi(^{\circ})$ | 20.60 | | 54.49 | | 54.26 | |
| $\theta(^{\circ})$ | 58.30 | | 32.63 | | 37.7 | |

Table 2: Mean absolute and mean absolute percentage error between dipole model prediction and measured magnetic fields

7 Conclusion and Recommendation

This project is aimed at characterizing an 8-coil magnetic actuation system to control magnetic surgical tools in a three-dimensional operating space. The magnetic field generated by the coil system is found to be in the linear magnetization range from a preliminary measurement. As a result, a principle of superposition is used by measuring the magnetic field of each coil with 2A input current increment in the range of $\pm 15A$. To measure the magnetic field, a 4×4 array of MLX90393 magnetic flux sensors is attached to Franka Emika robot arm to precisely move through 3D grid points of the operating space. The magnetic field measurement has been successfully collected, processed, and stored to be utilized for validation and model training. By combining the effects of each coil's magnetic field, it was demonstrated that it is possible to obtain over 2.5 billion sweeps of data. If interpolation between current inputs is considered, the amount of data that can

be obtained is unlimited. The measured dataset was also used to assess the dipole model prediction which suggests that more tweaking is required to better represent the generated field.

An important parameter to actuate surgical tools is the magnetic field gradient. In essence, it is the change in magnetic field with distance and more accurate values can be found from a fine resolution data than from the current measurement. Thus, it is left to be predicted after an ML model with fine resolution is trained.

A Equipment Specification

A.1 Sensors Specification

| Sensor | Manufacturer | Model | Range | Min. magnetic resolution ($\mu T/LSB$) | Mag-res- | Output |
|--------------------|-----------------------|--------------------------------|------------------|---|-----------------------------------|--------|
| Magnetometer (IMU) | Melexis | MLX90393 | 50mT – 5T | 3.220 in X and Y-axis and 5.672 in Z-axis | | 16 bit |
| Gaussmeter | Lakeshore Cryotronics | Model 460 3-channel Gaussmeter | $30\mu T$ to 30T | 30 ($\pm 0.1\%$ accuracy) | 5 $\frac{3}{4}$ -digit resolution | |

A.2 3D printer specification

| Model | Print resolution (microns) | | |
|------------------|----------------------------|--------|--------|
| | x-axis | y-axis | z-axis |
| UltiMaker | 6.9 | 6.9 | 2.5 |
| Formlabs Form 3+ | 25 | 25 | 25-300 |

B Calibration interface

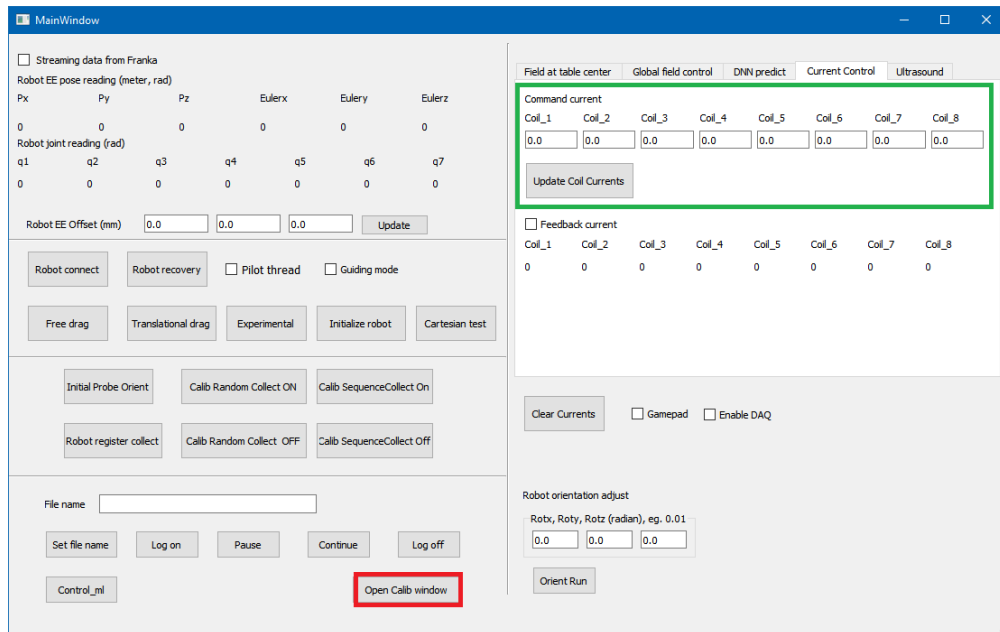


Figure 14: Main window

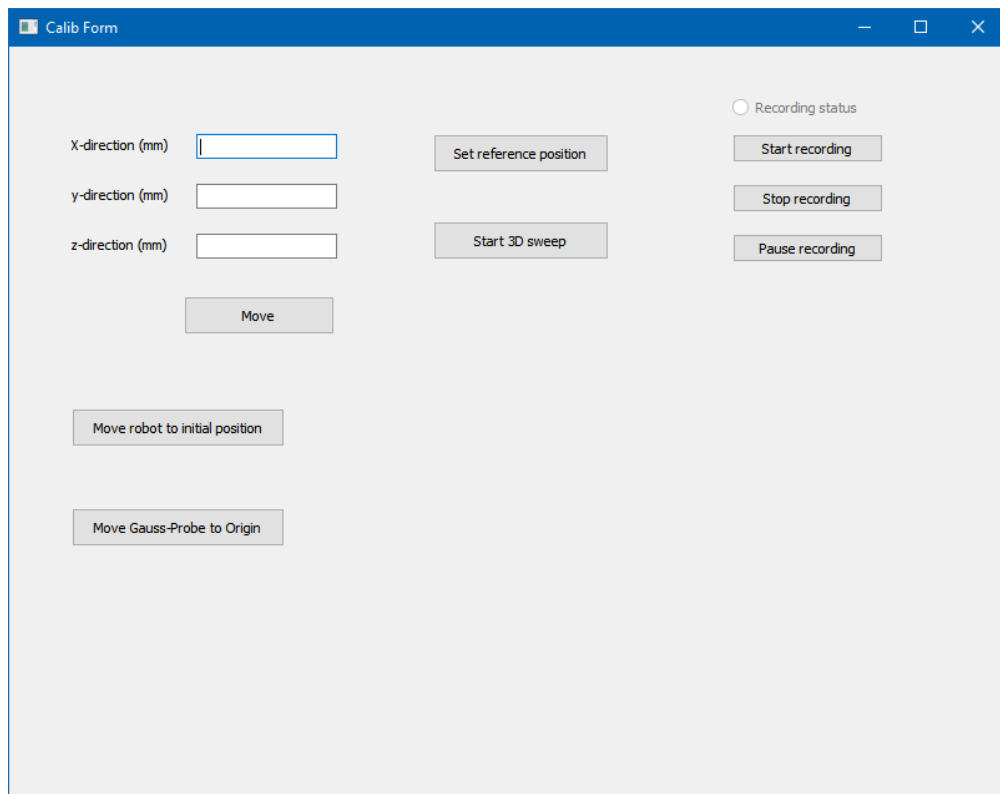
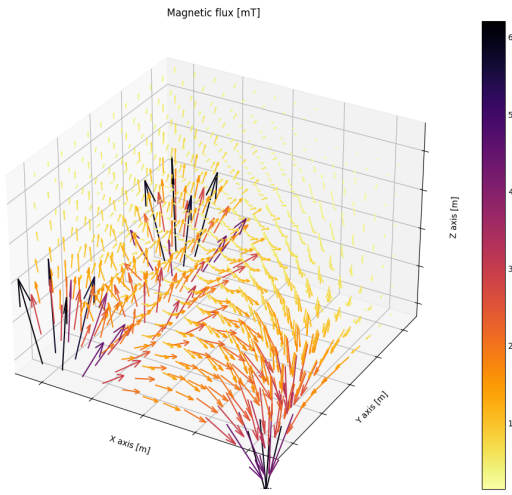
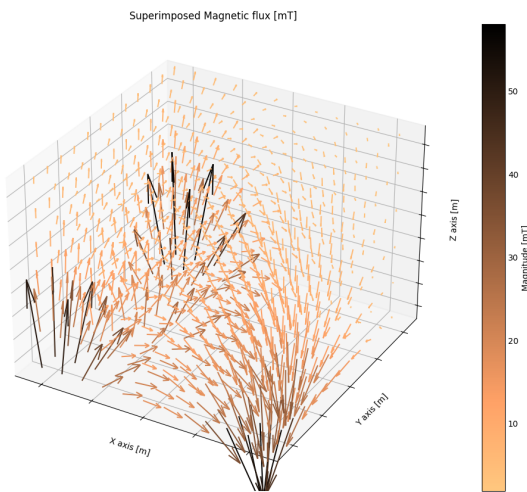


Figure 15: GUI interface for Calibration

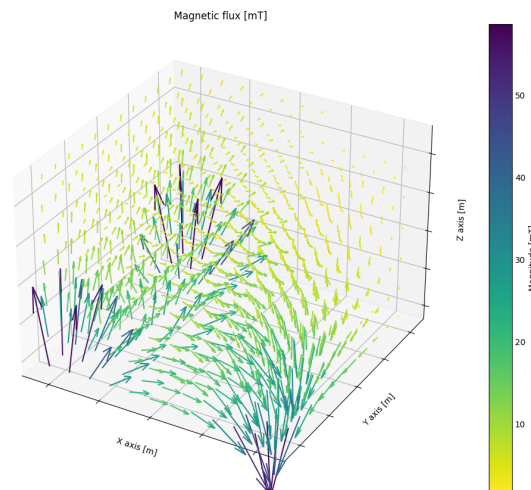
C Simulated vs Super-positioned vs measured data comparison



(a) Dipole model predicted magnetic field

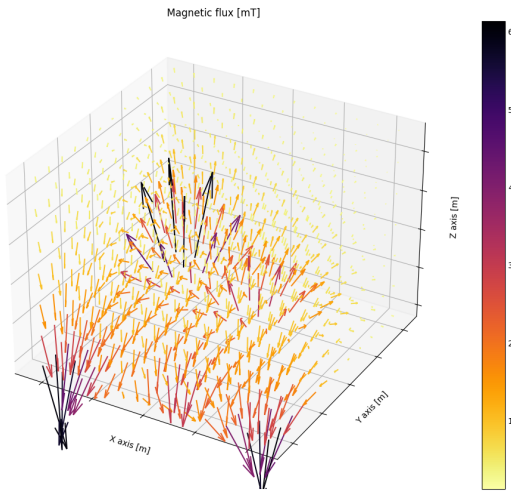


(b) Super-positioned magnetic field

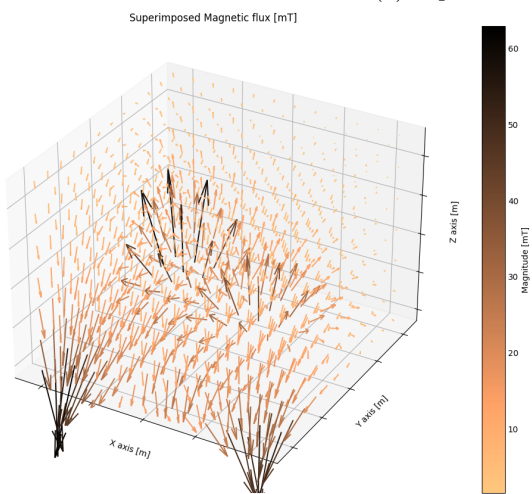


(c) Measured magnetic field

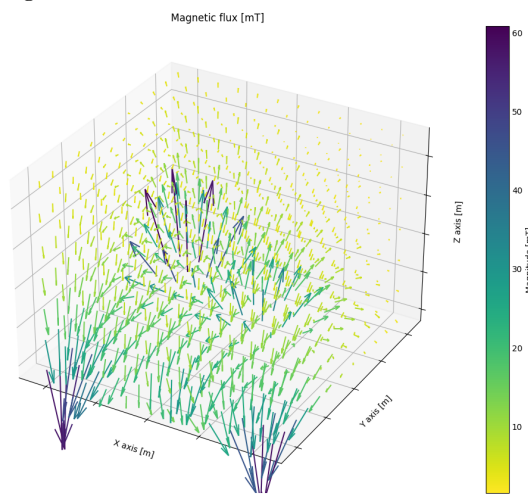
Figure 16: Simulated vs Super-positioned vs measured magnetic field data for test 2.
Input command current = $[10, 0, -10, -5, 5, 0, 0, 10]$ for coil 1 to 8 consecutively



(a) Dipole model predicted magnetic field



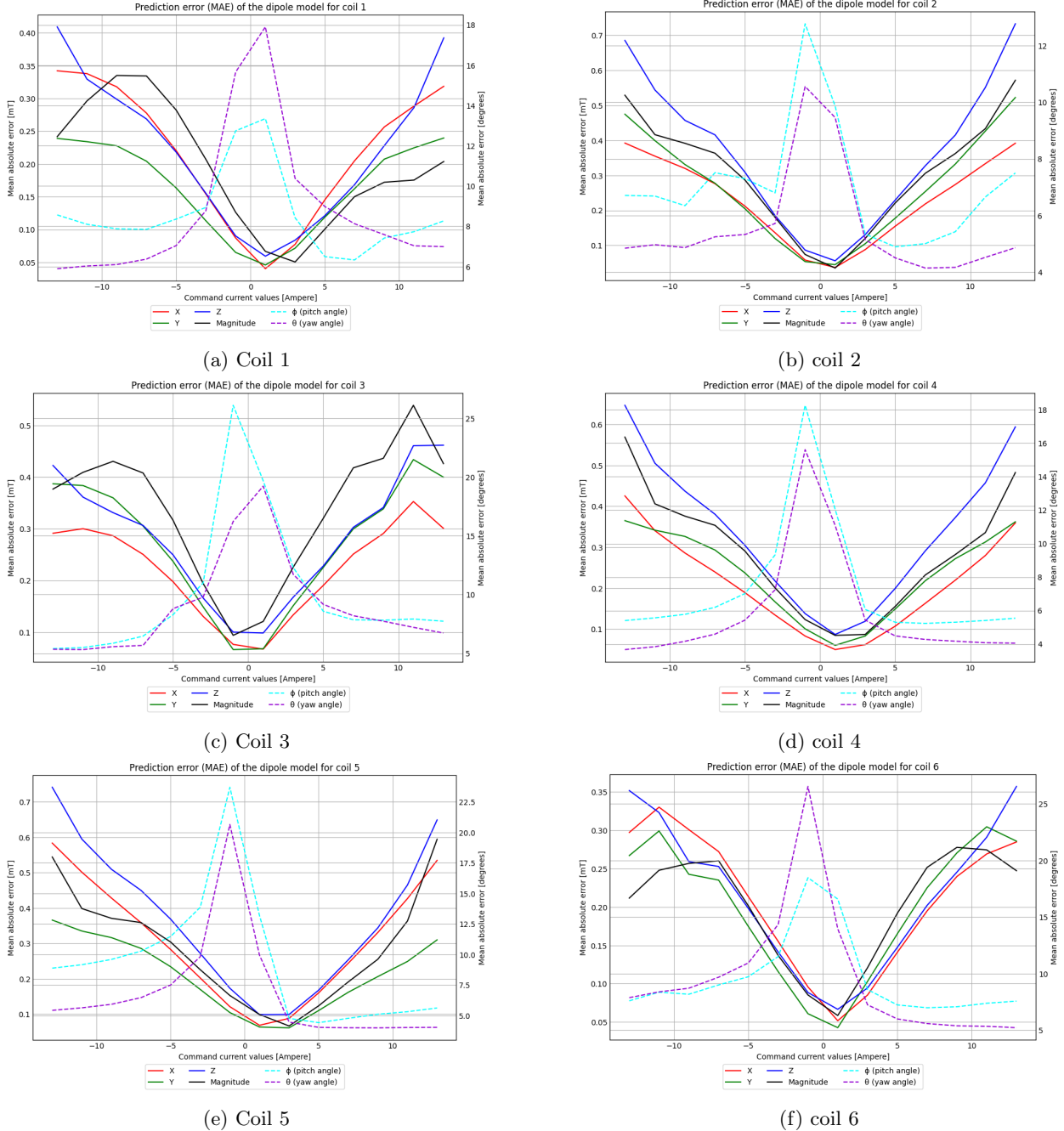
(b) Super-positioned magnetic field

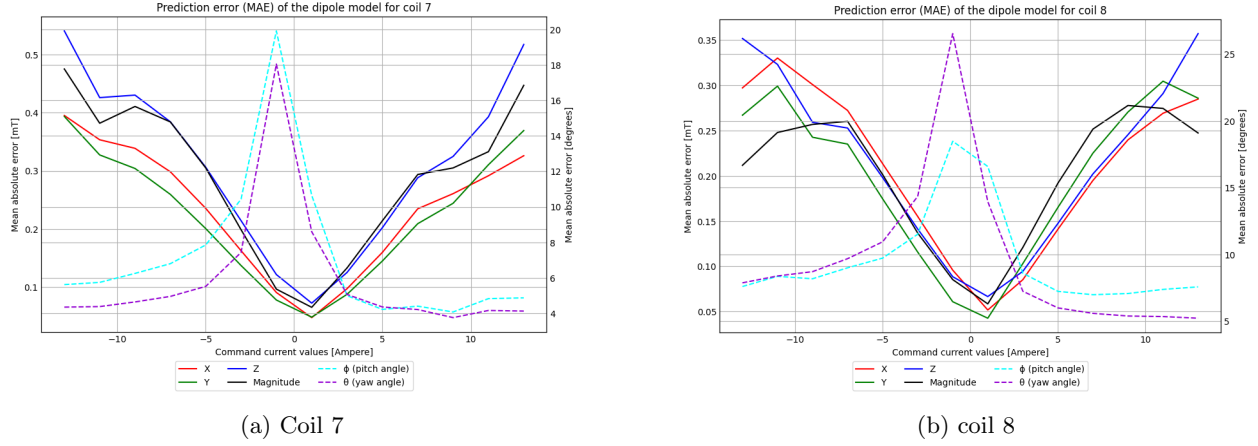


(c) Measured magnetic field

Figure 17: Simulated vs Super-positioned vs measured magnetic field data for test 3.
Input command current = $[-10, -5, -10, 0, 0, 0, 5, 10]$ for coil 1 to 8 consecutively

D Mean Average Error (MAE) of the dipole model





(a) Coil 7

(b) coil 8

Figure 19: Mean absolute error of the dipole model predication

References

- [1] A. Schonewille, *Maximizing workspace accessibility in magnetic actuation of tethered microsurgical tools using non-uniform magnetic fields*, 2022. [Online]. Available: <https://tspace.library.utoronto.ca/handle/1807/124773>.
- [2] D. J. Griffiths, *Introduction to electrodynamics*. Cambridge University Press, 2023.
- [3] A. A. Fard, “Deep learning based calibration for anisotropic electromagnetic navigation systems,” University of Toronto, Tech. Rep., 2023.
- [4] *Frank emika data sheet - robot arm and control*, April, 2020.
- [5] M. P. Kummer, J. J. Abbott, B. E. Kratochvil, R. Borer, A. Sengul, and B. J. Nelson, “Octomag: An electromagnetic system for 5-dof wireless micromanipulation,” *IEEE Transactions on Robotics*, vol. 26, no. 6, pp. 1006–1017, 2010.